

Perovskites

International Edition: DOI: 10.1002/anie.201910617

German Edition: DOI: 10.1002/ange.201910617

An All-Inorganic Perovskite-Phase Rubidium Lead Bromide Nanolaser

Bing Tang⁺, Yingjie Hu⁺, Hongxing Dong,^{*} Liaoxin Sun, Binbin Zhao, Xiongwei Jiang, and Long Zhang^{*}

Abstract: Rubidium lead halides ($RbPbX_3$), an important class of all-inorganic metal halide perovskites, are attracting increasing attention for photovoltaic applications. However, limited by its lower Goldschmidt tolerance factor $t \approx 0.78$, all-inorganic $RbPbBr_3$ has not been reported. Now, the crystal structure, X-ray diffraction (XRD) pattern, and band structure of perovskite-phase $RbPbBr_3$ has now been investigated. Perovskite-phase $RbPbBr_3$ is unstable at room temperature and transforms to photoluminescence (PL)-inactive non-perovskite. The structural evolution and mechanism of the perovskite–non-perovskite phase transition were clarified in $RbPbBr_3$. Experimentally, perovskite-phase $RbPbBr_3$ was realized through a dual-source chemical vapor deposition and annealing process. These perovskite-phase microspheres showed strong PL emission at about 464 nm. This new perovskite can serve as a gain medium and microcavity to achieve broadband (475–540 nm) single-mode lasing with a high Q of about 2100.

All-inorganic metal halide perovskites of the form $CsPbX_3$ ($X = Cl, Br, I$), owing to their remarkable properties, are attracting increasing attention for use in optoelectronic devices such as solar cells, light-emitting diodes (LEDs), and semiconductor nanolasers.^[1–10] Such all-inorganic perovskites exhibit superior properties, including improved photo-

and thermo-stability, higher resistance to the atmosphere, and enhanced exciton binding energies.^[11–18] In fact, few potential alternatives can realize all-inorganic ABX_3 perovskites except those containing Cs^+ . This is because the ionic radius of A must exceed the threshold value of the Goldschmidt tolerance factor $t \approx 0.8$. The Goldschmidt tolerance factor, $t = (r_A + r_X) / \sqrt{2}(r_B + r_X)$, describes the formability and stability of the perovskite structure, where r_A , r_B , and r_X represent the radii of the A, B, and X ions, respectively.^[19,20] The ideal tolerance factor t of a perovskite structure is 0.8–1, resulting in few alternative choices for the A cation. In fact, many perovskite compounds have a tolerance factor lower than 0.8; this indicates that the perovskite structure is hard to realize and readily transforms to non-perovskite phase.^[21–23] That is why few A cations can fit into the network of MX_6 octahedra to realize all-inorganic perovskites.

Rubidium (Rb), the neighbor alkali element of cesium (Cs), is another potential choice for the A cation to realize all-inorganic perovskites of the form ABX_3 . More importantly, the $RbPbBr_3$ perovskite may exhibit novel optoelectronic properties and help us understand the structure–property relationship of the perovskite family. In fact, great efforts have been devoted toward the exploration of Rb-based perovskites. Up to now, Rb/Cs mixed perovskites have been reported to show better photovoltaic performance.^[23–26] $Rb_xCs_{1-x}PbBr_3$ perovskite quantum dots were found to exhibit high quantum yield (93%), narrower photoluminescence (PL) emission linewidth (18–27 nm), and excellent wide color gamut coverage.^[27–31] However, all-inorganic perovskite $RbPbBr_3$ structures have still not been realized. Theoretical stability, as indicated by the tolerance factor t , should be considered carefully for the realization of the all-inorganic $RbPbBr_3$ perovskite. The tolerance factor of $RbPbBr_3$ is about 0.78 (the effective ionic radii of Rb^+ , Pb^{2+} , and Br^- are 1.61, 1.19, and 1.96 Å, respectively). This indicates that $RbPbBr_3$ perovskite structures are hard to realize and have poor stability.^[23,28,30,31] The incorporation of Cs^+ into $RbPbBr_3$ will lead to a larger tolerance factor and stabilize the perovskite phase. Woodward and Chen et al. thus obtained $Rb_xCs_{1-x}PbBr_3$ perovskite quantum dots.^[30,31] So far, the realization of the all-inorganic perovskite $RbPbBr_3$ is still a great challenge. A new preparation strategy should be developed for the realization of all-inorganic $RbPbBr_3$ perovskite structures.

In this work, to realize all-inorganic perovskite-phase $RbPbBr_3$, a new preparation strategy combining a dual-source chemical vapor deposition and a high-temperature annealing process is developed. The crystal structures, XRD patterns, and band structures of the perovskite and non-perovskite

[*] B. Tang,^[†] Prof. H. Dong, Prof. X. Jiang, Prof. L. Zhang
Key Laboratory of Materials for High-Power Laser, Shanghai Institute of Optics and Fine Mechanics, Chinese Academy of Sciences
Shanghai, 201800 (China)
E-mail: hongxingd@siom.ac.cn
lzhang@siom.ac.cn

B. Tang^[†]
Center of Materials Science and Optoelectronics Engineering,
University of Chinese Academy of Sciences
Beijing, 100049 (China)

Y. Hu^[†]
Key Laboratory of Advanced Functional Materials of Nanjing,
Nanjing Xiaozhuang University
Nanjing, 211171 (China)

Prof. L. Zhang
IFSA Collaborative Innovation Center, Shanghai Jiao Tong University
Shanghai, 200240 (China)

Dr. L. Sun, B. Zhao
National Lab for Infrared Physics, Shanghai Institute of Technical
Physics, Chinese Academy of Sciences
Shanghai, 200083 (China)

[†] These authors contributed equally to this work.

Supporting information and the ORCID identification number(s) for the author(s) of this article can be found under:
<https://doi.org/10.1002/anie.201910617>.

RbPbBr₃ were theoretically analyzed. The simulation results showed that perovskite-phase RbPbBr₃ is unstable at room temperature and easily transforms to a PL-inactive non-perovskite structure. Furthermore, we clarified the perovskite–non-perovskite phase-transition mechanism in RbPbBr₃. This explains why perovskite-phase RbPbBr₃ has not yet been obtained. Based on our strategy, we obtained perovskite-phase RbPbBr₃ microspheres with regular spherical structures, smooth surfaces, and strong PL emission at about 464 nm. Such microspheres can be used as a whispering gallery mode (WGM) microcavity for nanolasing. Single-mode lasing with a lasing threshold of $P \approx 17.8 \mu\text{J cm}^{-2}$ and a high-quality factor Q of about 2100 was achieved in these RbPbBr₃ microspheres. Furthermore, single-mode lasing can be tuned continually from 475–540 nm by adjusting the cavity size and the substitution of monovalent cation Rb with Cs.

Three crystal structures including cubic, tetragonal, and orthorhombic, are widely reported for lead-halide perovskites. The tolerance factor of RbPbBr₃ is about 0.78; this indicates that RbPbBr₃ may be obtained with either perovskite or non-perovskite structure of the orthorhombic phase. We reconstructed the exact crystal structures of perovskite and non-perovskite RbPbBr₃ from their isostructures.^[32,33] The exact crystal structural parameters of RbPbBr₃ in perovskite and non-perovskite phases, respectively, are given in the Supporting Information, Tables S1 and S2. They were calculated using density functional theory (DFT) methods. Figure 1 a,b depict the crystal structures of perovskite- and non-perovskite-phase RbPbBr₃. Both phases consist of an orthorhombic phase with *Pnma* symmetry and involve a distorted rotation of the [PbBr₆]⁴⁺ octahedral units compared with the cubic structure.^[21,22] The main part of the

perovskite and non-perovskite crystal structures is the [PbBr₆]⁴⁺ octahedral unit, which is formed with one Pb and six coordinated Br atoms. Additionally, Rb atoms sit at the vacant position of the [PbBr₆]⁴⁺ octahedra in the network. Theoretical calculation of the Gibbs free energy at different temperatures is shown in the Supporting Information, Figure S1. The simulation results show that the perovskite phase of RbPbBr₃ is unstable at room temperature and can be obtained at temperatures above 147°C. The formation of the perovskite phase of RbPbBr₃ is realized through atomic rearrangement from the non-perovskite phase with the NH₄CdCl₃-type structure. Theoretical XRD patterns of perovskite- and non-perovskite-phase RbPbBr₃ are shown in Figures 1 c and d; these patterns were calculated using the Reflex module of Material Studio software. To analyze the optoelectronic properties of RbPbBr₃, the electronic structures and partial density of states (PDOS) of perovskite- and non-perovskite-phase RbPbBr₃ were calculated using density functional theory. In Figures 1 e and f, it can be clearly seen that perovskite-phase RbPbBr₃ has a direct band gap of 2.63 eV, while the non-perovskite phase shows an indirect band gap of 3.04 eV. According to the distribution of the PDOS, the minimum of the conduction band (CBM) and the maximum of the valence band (VBM) of perovskite-phase RbPbBr₃ are mainly dominated by the Pb 6p and Br 4p orbitals, just as in the non-perovskite-phase RbPbBr₃, while the orbital of Rb has less influence on the band structure. So far, the crystal structures, XRD patterns, and band structures of perovskite and non-perovskite RbPbBr₃ have been theoretically analyzed. Theoretical simulation results revealed that perovskite-phase RbPbBr₃ with good optical properties can be realized at high temperatures.

Experimentally, perovskite-phase RbPbBr₃ was obtained through a dual-source chemical vapor deposition and a high-temperature annealing process at 290°C. Non-perovskite RbPbBr₃ microspheres were prepared first through a one-step dual-source chemical vapor process. These samples were then annealed at 290°C for 1 h to obtain perovskite structures. Detailed information regarding this process can be found in the experimental section. Low- and high-magnification scanning electron microscopy (SEM) images of the as-synthesized perovskite microspheres are shown in Figure 2 a. RbPbBr₃ microspheres with a diameter D of about 1.2 μm were uniformly distributed on the silicon sub-

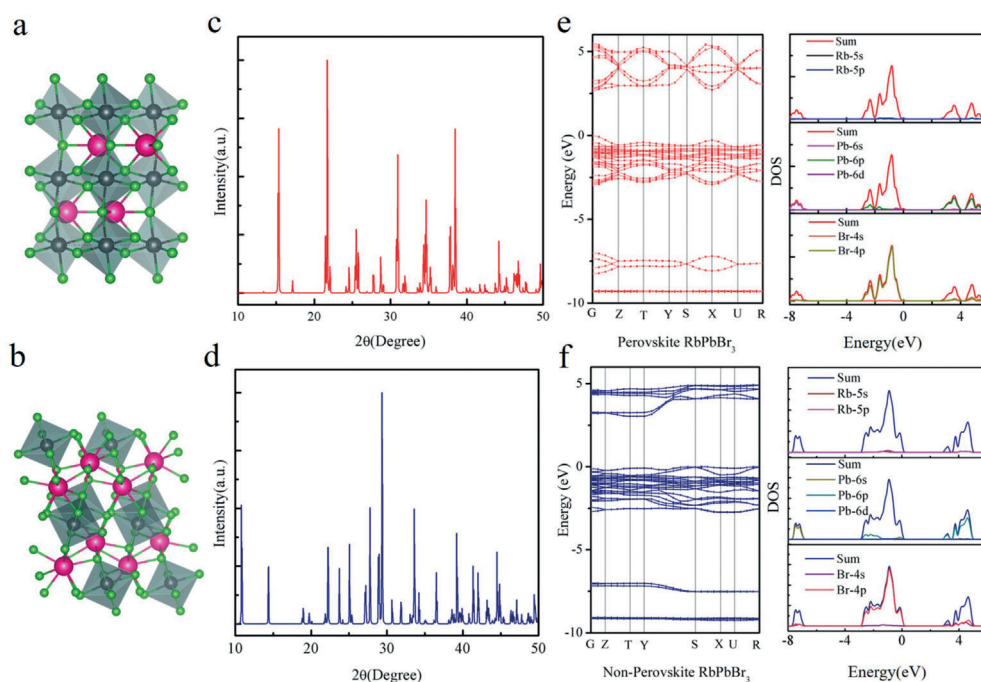


Figure 1. Theoretical simulation of the crystal structures, XRD patterns, energy band structures, and partial density of states (PDOS) of RbPbBr₃ with perovskite (a,c,e) and non-perovskite (b,d,f) phases. In (a) and (b): The Rb⁺ pink, Pb²⁺ gray, Br⁻ green.

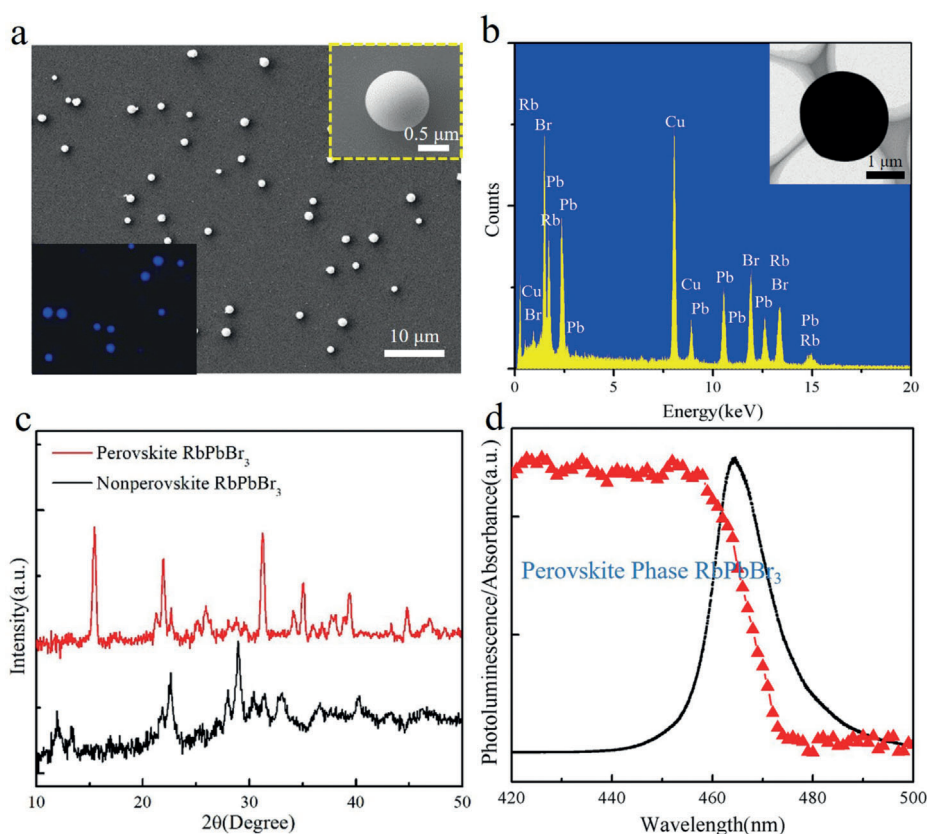


Figure 2. a) Typical SEM images of the perovskite-phase RbPbBr₃ microspheres. Top inset: The magnified image of an individual RbPbBr₃ microsphere. Left inset: PL images of the perovskite RbPbBr₃ microspheres. b) Energy-dispersive X-ray spectroscopy of a RbPbBr₃ microsphere. Right inset: TEM image of single RbPbBr₃ microsphere. c) X-ray diffraction results of perovskite and non-perovskite RbPbBr₃ samples. d) Photoluminescence and absorption spectra of the RbPbBr₃ microsphere with perovskite phase.

strate. It can be clearly seen that most microspheres show regularly spherical structures and smooth surfaces; this makes them ideal candidates for whispering gallery mode (WGM) microcavities. In the left inset of Figure 2a, uniformly blue PL emission can be observed from these perovskite-phase RbPbBr₃ microspheres. A typical transmission electron microscopy (TEM) image of single RbPbBr₃ microsphere is shown in the inset of Figure 2b, confirming its regularly spherical morphology from the clear contrast. The formation of RbPbBr₃ was confirmed by the energy-dispersive X-ray (EDX) spectroscopy results shown in Figure 2b, which presents a molar ratio of Rb/Pb/Br of about 1:1.03:2.99. The X-ray diffraction patterns of RbPbBr₃ in Figure 2c confirm the phase transition from non-perovskite to perovskite at 290 °C, which agrees well with theoretical simulations. According to the XRD results in Figures 2c, Figures 1c and d, the non-perovskite phase dominates in the directly obtained samples; the main phase of the annealed samples was transformed to a perovskite structure.^[30,31] Figure 2d depicts the PL and absorption spectra of perovskite-phase RbPbBr₃. Interestingly, the perovskite-phase RbPbBr₃ microspheres showed strong PL emission at about 464 nm with a full width at half maximum (FWHM) of about 12.4 nm, while the non-perovskite RbPbBr₃ samples were PL-inactive.

This is consistent with the theoretical simulation results in Figures 1e and f, which show direct and indirect band gaps for the perovskite and non-perovskite phases of RbPbBr₃, respectively. The absorption edge of perovskite-phase RbPbBr₃ is located at about 460 nm, and thus the band gap is about 2.70 eV, which agrees well with the PL peak and simulated results. So far, these results experimentally demonstrate the phase transition of RbPbBr₃ from non-perovskite to perovskite. These perovskite-phase samples have regularly spherical geometry, smooth surfaces, and strong PL emission. Such perovskite microspheres will be good candidates for WGM microcavities and gain medium to achieve nanolasing.

To gain insight into the phase-transition mechanism, the structural evolution details were analyzed. Figure 3a depicts the reversible phase change between the perovskite and non-perovskite structures of RbPbBr₃. The perovskite structure is formed by annealing a non-perovskite sample at 290 °C for 1 h in a N₂-filled environment. Similar to all-inorganic cesium lead halide perovskites, the perovskite phase of RbPbBr₃ is kinetically trapped and metastable in a N₂-filled environment when cooled to room temperature.^[34,35] When exposed to a natural environment, perovskite samples undergo a reconstructive phase transition to a non-perovskite phase. During the reconstructive process, [PbBr₆]⁴⁺ octahedra undergoes a transition from a corner-sharing structure to an edge-sharing structure. The detailed structural evolution process can be observed in the video provided in the Supporting Information. The typical structural evolution on the existence of a Br vacancy is shown in Figure 3b. It can be clearly seen that the whole process consists of the tilting of the octahedral unit, the breaking of a Pb–Br bond, and the recombination of a Pb–Br bond. Furthermore, the formation of the non-perovskite structure is also accompanied by the reorientation of Rb (see Figure 3c). As shown in Figure 3c, the Rb atom is surrounded by three adjacent Pb₂Br₁₀ chains in the non-perovskite structure. We also found that no perovskite–non-perovskite phase transition took place when annealing a perovskite sample in a N₂-filled environment at temperatures between 30–290 °C for 1 h. A RbPbBr₃ sample stored in a N₂-filled environment at room temperature can maintain the perovskite phase for about 1 month or even longer. The XRD data is shown in the Supporting Information, Figure S2. However,

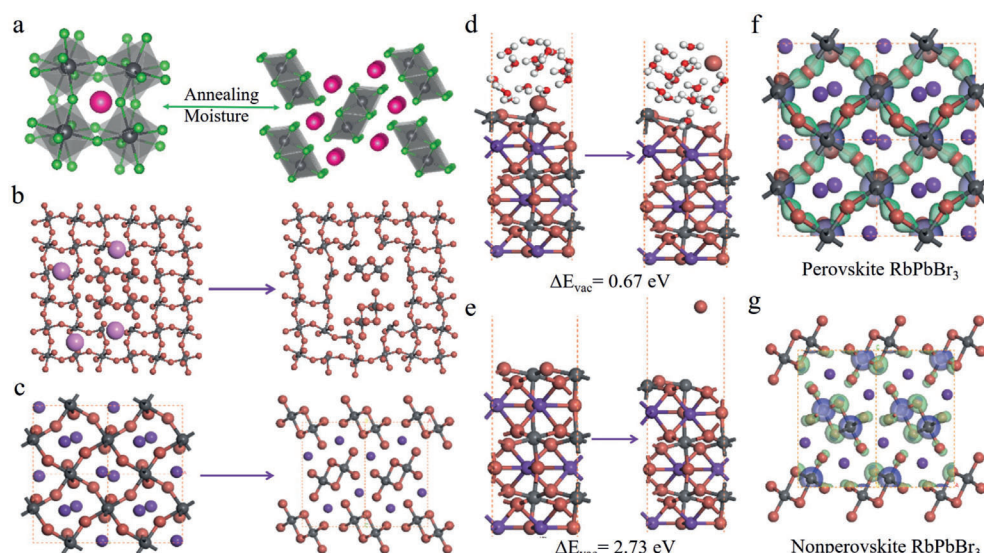


Figure 3. Mechanism of the phase transition. a) The reversible phase transition between the perovskite and non-perovskite structures. The Rb^+ pink, Pb^{2+} gray, Br^- green. b) The structural evolution from $\text{Pb}_2\text{Br}_{20}$ to couple $\text{Pb}_2\text{Br}_{10}$ on the existence of Br vacancies (pink sphere). Rb is not shown for simplicity. c) The structure transformation from the perovskite to non-perovskite observed from [010] crystal surface. d), e) The comparison of a Br vacancy formation energy in moisture ($\Delta E_{\text{vac}} = 0.67$ eV) and vacuum ($\Delta E_{\text{vac}} = 2.73$ eV) conditions. f), g) Representation of the orbital arrangements for perovskite- and non-perovskite-phase RbPbBr_3 . VBM and CBM orbitals are represented by green and blue, respectively. The isosurface value is set to be $0.018 \text{ e}\text{\AA}^{-3}$. The Rb^+ , Pb^{2+} , and Br^- ions in (b)–(e) are represented by violet, gray, and reddish-brown spheres.

freshly prepared perovskite samples will degrade in about 20 min when exposed to the natural environment. DFT calculations were carried out to clarify these differences. As shown in Figure 3d,e, the presence of water molecules reduces the formation energy of a Br vacancy to $\Delta E_{\text{vac}} \approx 0.67$ eV; this will further lower the free-energy barrier of nucleation (Figure 3b) and accelerate the phase transition at room temperature.^[36,37] In Figures 3f and g, it can be seen that the VBM and CBM orbitals of RbPbBr_3 are significantly shifted during the phase-transition process, resulting in distinct optical properties. These results clarified the phase-transition mechanism and the direct–indirect band gap transition of RbPbBr_3 .

The optically pumped lasing properties of perovskite-phase RbPbBr_3 microspheres were probed through a home-built confocal microphotoluminescence system. As presented in Figure 4a, a femtosecond laser with a wavelength of 400 nm was used as the pumping source to excite single RbPbBr_3 perovskite microsphere. The waist of the pulsed laser beam was about $3 \mu\text{m}$ to pump the whole RbPbBr_3 microsphere homogeneously. The perovskite-phase RbPbBr_3 microsphere acts as both a gain medium and WGM microcavity. At a high pump density, the gain just balances or exceeds the optical losses and a single-mode lasing at 475.6 nm can be observed. Figure 4b presents a two-dimensional (2D) pseudo-color plot recorded from a single RbPbBr_3 microsphere with $D \approx 1.2 \mu\text{m}$ as a function of pump density. By increasing the pump density from 5 to $100 \mu\text{J cm}^{-2}$, the transition from broadband emission to a sharp peak could be clearly observed. This indicates the occurrence of lasing action. Figure 4c depicts typical PL

emission spectra near the lasing threshold. When the pump density P was about $13.2 \mu\text{J cm}^{-2}$ (below the lasing threshold), a broad emission peak at about 466 nm with a FWHM of about 15.8 nm was observed; this can be attributed to spontaneous emission. When P reached the lasing threshold of about $17.8 \mu\text{J cm}^{-2}$, a sharp peak with narrow linewidth appeared above the background. As the pump density was continually increased, the intensity of the lasing peak at about 475.6 nm grew rapidly while the PL emission remained almost constant. This confirms the realization of single-mode lasing. As P reached the lasing threshold, the FWHM of the emission spectrum quickly dropped from 15.8 to about

0.23 nm, which also supports the appearance of lasing action. It was noticed that the peak position of single-mode lasing was blue-shifted with increasing pump density. This might have resulted from band filling, thermo-optics, or electron/hole many-body interactions.^[38,39] Figure 4d shows the integrated PL intensity as a function of pump density. These log–log plots show the S-curve model of lasing oscillation with two kinks at 17.8 and $30.1 \mu\text{J cm}^{-2}$, respectively.^[40] As the pump density increases, the evolution from spontaneous emission to simulated emission occurs at $17.8 \mu\text{J cm}^{-2}$, and gain saturation starts at $30.1 \mu\text{J cm}^{-2}$. Such behavior clarifies the achievement of single-mode lasing, giving the lasing threshold at about $17.8 \mu\text{J cm}^{-2}$. Figure 4e depicts single-mode lasing at about 475.6 nm, and a Lorentzian curve with $\delta\lambda \approx 0.23$ nm is used to fit these plots. According to the equation $Q = \lambda/\delta\lambda$, the quality factor of single-mode lasing at 475.6 nm was calculated to be $Q \approx 2100$, which is higher than most reported nanolasing systems, including microdisks, nanowires, and nanorods. The spherical shape of the perovskite RbPbBr_3 microsphere makes them ideal WGM candidates for total internal reflection, and ensures lower optical losses.^[41–45] Therefore, the achievement of single-mode lasing with a high Q factor is mainly attributed to the excellent WGM cavity structure.

The lasing behaviors of a series of RbPbBr_3 microspheres were investigated to clarify the influence of microcavity size on optical confinement and lasing properties. Figure 5a presents single-mode lasing spectra recorded from different RbPbBr_3 microspheres. As the diameter increased from 1156 to 1260 nm, single-mode lasing was red-shifted from 471.2 to 478.9 nm. Detailed information about single-mode lasing at

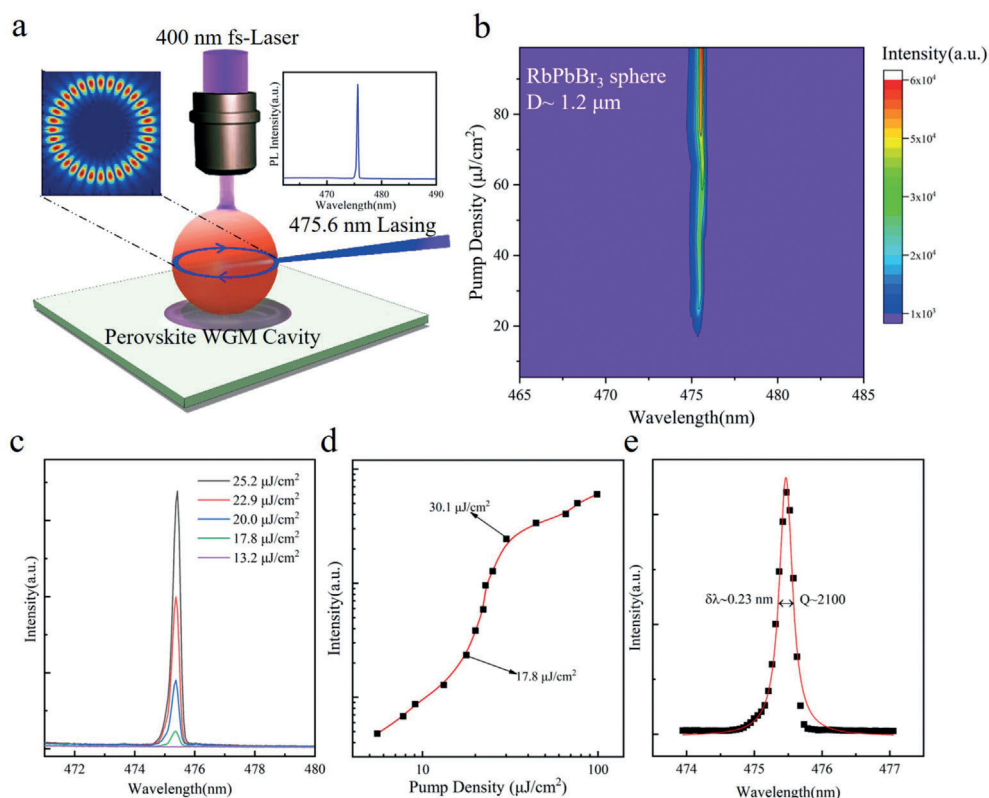


Figure 4. a) An individual RbPbBr₃ microsphere pumped by a 400 nm fs-laser (ca. 40 fs, 10 kHz). The light path inside the spherical cavity is signaled by the blue circle. b) 2D pseudo-color plot of a RbPbBr₃ microsphere under different pump density. c) The PL spectra recorded from single RbPbBr₃ microsphere around the lasing threshold. Inset: Photoluminescence image recorded around the lasing threshold. d) The integrated PL intensity is plotted as a function of pump density, giving the lasing threshold at about 17.8 $\mu\text{J cm}^{-2}$. e) Lorentz fitting of the single-mode lasing at about 475.6 nm, giving a FWHM ($\delta\lambda$) \approx 0.23 nm, the corresponding Q factor is about 2100.

471.2 nm can be found in the Supporting Information, Figure S3. The wavelength of lasing in a spherical resonator has been theoretically and experimentally demonstrated as:^[9,42–47]

$$\lambda \approx \pi D N \nu \quad (1)$$

where ν and λ describe the mode number and wavelength of the lasing peak, respectively, while D and N are the diameter and refractive index of the spherical microcavity, respectively. Figure 5b plots the peak position of single-mode lasing as a function of the diameter of the microsphere. The single-mode lasing wavelength is continuously red-shifted with increasing cavity size. A linear curve can be used to fit these plots in Figure 5b, which agrees well with the theoretical prediction from the above equation. To deeply decouple the modulation effect of the microcavity, optical mode simulations were carried out using the finite domain time difference (FDTD) solution. The inset of Figure 5b shows the simulation results for single-mode lasing at about 475.6 nm; it can be clearly seen that the electrical field is well-confined inside. The simulated electrical field distributions of other perovskite RbPbBr₃ microspheres can be found in the Supporting Information, Figure S4. A spherical microcavity shows perfect successive total internal reflection and ensures lower optical losses compared with other types of microcavity, such

as squares, hexagonals, or other shapes.^[41–47] That is why most spherical microcavities have excellent lasing performance. The band gap of APbX₃ perovskites is mainly dependent on the [PbX₆]⁴⁺ octahedral unit, while the A cation influences the band structure by changing the bonding properties between the Pb and X atoms of the octahedra.^[21,22]

Rb_xCs_{1-x}PbBr₃ microspheres also can be obtained through a chemical vapor deposition process. Figure 5c depicts the PL images and spectra of as-prepared samples. Uniformly bright PL emission can be observed from these PL images. The PL emission peak was red-shifted from 464 to 529 nm as the ratio of Cs⁺ was increased. SEM and PL images of CsPbBr₃ microspheres are presented in the Supporting Information, Figure S5. As shown in Figure 5d, high- Q single-mode lasing can be tuned from blue to green

(475–540 nm) in these perovskite microspheres. In the insets of Figure 5d, clear interference patterns can be observed from the PL images under a high pump density; this indicates the formation of WGM lasing.

In conclusion, perovskite-phase RbPbBr₃ was realized through a chemical vapor deposition and a high-temperature annealing process. The crystal phase, XRD pattern, and band structure of perovskite RbPbBr₃ were investigated theoretically. Theoretical results showed that perovskite-phase RbPbBr₃ is difficult to obtain directly because of the instability of its phase structure at room temperature. The perovskite–non-perovskite structural evolution was systematically analyzed to reveal the mechanism of the phase transition of RbPbBr₃. We obtained perovskite-phase RbPbBr₃ with regular spherical structures, smooth surfaces, and strong PL emission at about 464 nm through this new strategy. We found that these new perovskite samples can act both as a gain medium and microcavity to achieve single-mode lasing with a high Q of about 2100. By modulating the microcavity size and/or the ratio of monovalent cation, single-mode lasing can be tuned continuously from blue to green (475–540 nm). Our work provides a simple way to achieve perovskite-phase RbPbBr₃ with superior optical properties, which may be used as a promising candidate for micro/nanolasers.

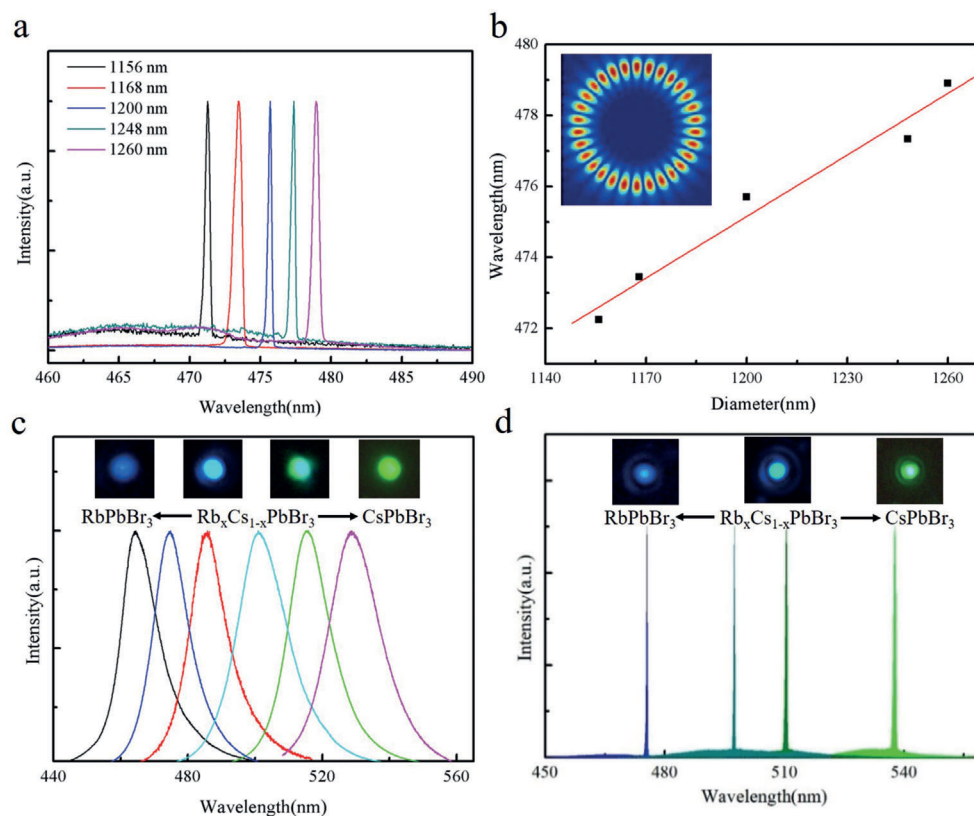


Figure 5. a) Single-mode lasing recorded from five typical RbPbBr₃ microspheres. b) The relationship between the wavelength of single-mode lasing and the diameter of RbPbBr₃ microsphere. Top inset: Simulated electric field distribution of single-mode lasing at about 475.6 nm. c) Photoluminescence images and spectra of RbPbBr₃, Rb_xCs_{1-x}PbBr₃, CsPbBr₃ microspheres. d) Single-mode lasing recorded from single Rb_xCs_{1-x}PbBr₃ microsphere. Insets: Photoluminescence images of perovskite microspheres under a high pump density.

Acknowledgements

This work was supported financially by the NSFC (61675219, 61875256, 11674343, 91750103). H.D. acknowledges the Youth Top-notch Talent Support Program in Shanghai. We thank Q. Si for helping design and draw the picture in Figure 4a and TOC.

Conflict of interest

The authors declare no conflict of interest.

Keywords: all-inorganic perovskite phases · nanolasers · rubidium lead bromide

- [1] T. Zhang, M. I. Dar, G. Li, F. Xu, N. Guo, M. Grätzel, Y. Zhao, *Sci. Adv.* **2017**, *3*, e1700841.
- [2] W. J. Yin, T. Shi, Y. Yan, *Adv. Mater.* **2014**, *26*, 4653.
- [3] J. Song, J. Li, X. Li, L. Xu, Y. Dong, H. Zeng, *Adv. Mater.* **2015**, *27*, 7162.
- [4] Q. Zhang, R. Su, X. Liu, J. Xing, T. C. Sum, Q. Xiong, *Adv. Funct. Mater.* **2016**, *26*, 6238.
- [5] Y. Fu, H. Zhu, C. C. Stoumpos, Q. Ding, J. Wang, M. G. Kanatzidis, X. Zhu, S. Jin, *ACS Nano* **2016**, *10*, 7963.

- [6] H. Zhou, S. Yuan, X. Wang, T. Xu, X. Wang, H. Li, W. Zheng, P. Fan, Y. Li, L. Sun, A. Pan, *ACS Nano* **2017**, *11*, 1189.
- [7] X. Wang, M. Shoaib, X. Wang, X. Zhang, M. He, Z. Luo, W. Zheng, H. Li, T. Yang, X. Zhu, L. Ma, A. Pan, *ACS Nano* **2018**, *12*, 6170.
- [8] X. He, P. Liu, H. Zhang, Q. Liao, J. Yao, H. Fu, *Adv. Mater.* **2017**, *29*, 1604510.
- [9] B. Tang, H. Dong, L. Sun, W. Zheng, Q. Wang, F. Sun, X. Jiang, A. Pan, L. Zhang, *ACS Nano* **2017**, *11*, 10681.
- [10] K. Wang, S. Wang, S. Xiao, Q. Song, *Adv. Opt. Mater.* **2018**, *6*, 1800278.
- [11] Z. Wu, J. Chen, Y. Mi, X. Sui, S. Zhang, W. Du, R. Wang, J. Shi, X. Wu, X. Qiu, Z. Qin, Q. Zhang, X. Liu, *Adv. Opt. Mater.* **2018**, *6*, 1800674.
- [12] S. W. Eaton, M. Lai, N. A. Gibson, A. B. Wong, L. Dou, J. Ma, L. W. Wang, S. R. Leone, P. Yang, *Proc. Natl. Acad. Sci. USA* **2016**, *113*, 1993.
- [13] G. Xing, M. H. Kumar, W. K. Chong, X. Liu, Y. Cai, H. Ding, M. Asta, M. Grätzel, S. Mhaisalkar, N. Mathews, T. C. Sum, *Adv. Mater.* **2016**, *28*, 8191.
- [14] L. Huang, Q. Gao, L. D. Sun, H. Dong, S. Shi, T. Cai, Q. Liao, C. H. Yan, *Adv. Mater.* **2018**, *30*, 1800596.
- [15] Y. Wang, X. Sun, R. Shivanna, Y. Yang, Z. Chen, Y. Guo, G. C. Wang, E. Wertz, F. Deschler, Z. Cai, H. Zhou, T. M. Lu, J. Shi, *Nano Lett.* **2016**, *16*, 7974.
- [16] L. Protesescu, S. Yakunin, M. I. Bodnarchuk, F. Krieg, R. Caputo, C. H. Hendon, R. X. Yang, A. Walsh, M. V. Kovalenko, *Nano Lett.* **2015**, *15*, 3692.
- [17] Y. Wang, X. Li, J. Song, L. Xiao, H. Zeng, H. Sun, *Adv. Mater.* **2015**, *27*, 7101.

- [18] J. Chen, Y. Fu, L. Samad, L. Dang, Y. Zhao, S. Shen, L. Guo, S. Jin, *Nano Lett.* **2017**, *17*, 460.
- [19] V. M. Goldschmidt, *Naturwissenschaften* **1926**, *14*, 447.
- [20] M. A. Green, A. H. Baillie, H. J. Snaith, *Nat. Photonics* **2014**, *8*, 506.
- [21] B. R. Sutherland, E. H. Sargent, *Nat. Photonics* **2016**, *10*, 295.
- [22] Q. Zhang, S. Rui, W. Du, X. Liu, L. Zhao, S. T. Ha, Q. Xiong, *Small Methods* **2017**, *1*, 1700163.
- [23] M. Saliba, T. Matsui, K. Domanski, J. Y. Seo, A. Ummadisingu, S. M. Zakeeruddin, J. P. Correa-Baena, W. R. Tress, A. Abate, A. Hagfeldt, M. Grätzel, *Science* **2016**, *354*, 206.
- [24] Y. Hu, E. M. Hutter, P. Rieder, I. Grill, J. Hanisch, M. F. Aygüler, A. G. Hufnagel, M. Handloser, T. Bein, A. Hartschuh, K. Tvingstedt, V. Dyakonov, A. Baumann, T. J. Savenije, M. L. Petrus, P. Docampo, *Adv. Energy Mater.* **2018**, *8*, 1703057.
- [25] P. Yadav, M. I. Dar M, N. Arora, E. A. Alharbi, F. Giordano, S. M. Zakeeruddin, M. Grätzel, *Adv. Mater.* **2017**, *29*, 1701077.
- [26] M. Zhang, J. S. Yun, Q. Ma, J. Zheng, C. F. J. Lau, X. Deng, J. Kim, D. Kim, J. Seidel, M. A. Green, S. Huang, A. W. Y. Ho-Baillie, *ACS Energy Lett.* **2017**, *2*, 438.
- [27] H. Wu, Y. Yang, D. Zhou, K. Li, J. Yu, J. Han, Z. Li, Z. Long, J. Ma, J. Qiu, *Nanoscale* **2018**, *10*, 3429.
- [28] D. Amgar, T. Binyamin, V. Uvarov, L. Etgar, *Nanoscale* **2018**, *10*, 6060.
- [29] S. Baek, S. Kim, J. Y. Noh, J. H. Heo, S. H. Im, K. H. Hong, S. W. Kim, *Adv. Opt. Mater.* **2018**, *6*, 1800295.
- [30] J. W. Xiao, Y. Liang, S. Zhang, Y. Zhao, Y. Li, Q. Chen, *Chem. Eur. J.* **2019**, *25*, 2597.
- [31] M. R. Linaburg, E. T. McClure, J. D. Majher, P. M. Woodward, *Chem. Mater.* **2017**, *29*, 3507.
- [32] M. Rodová, J. Brožek, K. Knížek, *J. Therm. Anal.* **2003**, *71*, 667.
- [33] D. M. Trotsa, S. V. Myagkota, *J. Phys. Chem. Solids* **2008**, *69*, 2520.
- [34] J. Lin, M. Lai, L. Dou, C. S. Kley, H. Chen, F. Peng, J. Sun, D. Lu, S. A. Hawks, C. Xie, F. Cui, A. P. Alivisatos, D. T. Limmer, P. Yang, *Nat. Mater.* **2018**, *17*, 261.
- [35] M. Lai, Q. Kong, C. G. Bischak, Y. Yu, L. Dou, S. W. Eaton, N. S. Ginsberg, P. Yang, *Nano Res.* **2017**, *10*, 1107.
- [36] S. Dastidar, D. A. Egger, L. Z. Tan, S. B. Cromer, A. D. Dillon, S. Liu, L. Kronik, A. M. Rappe, A. T. Fafarman, *Nano Lett.* **2016**, *16*, 3563.
- [37] A. Mattoni, A. Filippetti, C. Caddeo, *J. Phys. Condens. Mater.* **2016**, *29*, 043001.
- [38] H. Zhu, Y. Fu, F. Meng, X. Wu, Z. Gong, Q. Ding, M. V. Gustafsson, M. T. Trinh, S. Jin, X. Y. Zhu, *Nat. Mater.* **2015**, *14*, 636.
- [39] G. Li, T. Che, X. Ji, S. Liu, Y. Hao, Y. Cui, S. Liu, *Adv. Funct. Mater.* **2019**, *29*, 1805553.
- [40] Q. Song, H. Cao, S. T. Ho, G. S. Solomon, *Appl. Phys. Lett.* **2009**, *94*, 061109.
- [41] H. Zhang, Q. Liao, X. Wang, J. Yao, H. Fu, *Adv. Opt. Mater.* **2016**, *4*, 1718.
- [42] B. Tang, L. Sun, W. Zheng, H. Dong, B. Zhao, Q. Si, X. Wang, X. Jiang, A. Pan, L. Zhang, *Adv. Opt. Mater.* **2018**, *6*, 1800391.
- [43] S. Yang, Y. Wang, H. Sun, *Adv. Opt. Mater.* **2015**, *3*, 1136.
- [44] A. Chiasera, Y. Dumeige, P. Féron, M. Ferrari, Y. Jestin, G. Nunzi Conti, S. Pelli, S. Soria, G. C. Righini, *Laser Photonics Rev.* **2010**, *4*, 457.
- [45] X. Wang, Q. Liao, H. Li, S. Bai, Y. Wu, X. Lu, H. Hu, Q. Shi, H. Fu, *J. Am. Chem. Soc.* **2015**, *137*, 9289.
- [46] Y. Liu, C. Xu, Z. Zhu, D. You, R. Wang, F. Qin, X. Wang, Q. Cui, Z. Shi, *Cryst. Growth Des.* **2018**, *18*, 5279.
- [47] W. Du, S. Zhang, Z. Wu, Q. Shang, Y. Mi, J. Chen, C. Qin, X. Qiu, Q. Zhang, X. Liu, *Nanoscale* **2019**, *11*, 3145.

Manuscript received: August 19, 2019

Accepted manuscript online: September 10, 2019

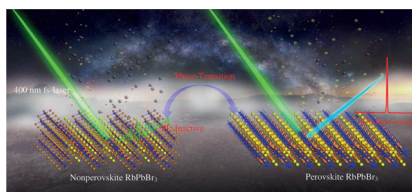
Version of record online: ■■■■■, ■■■■■

Communications

Perovskites

B. Tang, Y. Hu, H. Dong,* L. Sun, B. Zhao,
X. Jiang, L. Zhang* ——— ■■■■—■■■■

An All-Inorganic Perovskite-Phase
Rubidium Lead Bromide Nanolaser



All inorganic: The crystal structure, phase transition, band gap and optical properties of perovskite-phase RbPbBr_3 were analyzed theoretically and experimentally. This new perovskite microsphere can serve as a gain medium and microcavity to achieve broadband (475–540 nm) single-mode lasing with a high Q of about 2100.